MOCVD Epitaxy of β-$(Al_xGa_{1-x})_2O_3$ Thin Films on (010) Ga_2O_3 Substrates and N-type Doping

A F M Anhar Uddin Bhuiyan[1,a)], Zixuan Feng[1], Jared Johnson[2], Zhaoying Chen[1], Hsien-Lien Huang[2], Jinwoo Hwang[2], and Hongping Zhao[1,2,b)]

[1]*Department of Electrical and Computer Engineering, The Ohio State University, Columbus, OH 43210, USA*

[2]*Department of Materials Science and Engineering, The Ohio State University, Columbus, OH 43210, USA*

[a)]Email: bhuiyan.13@osu.edu; [b)]Corresponding author Email: zhao.2592@osu.edu

(010) β-$(Al_xGa_{1-x})_2O_3$ thin films were grown on (010) β-Ga_2O_3 substrates via metalorganic chemical vapor deposition (MOCVD) with up to 40% Al incorporation by systematic tuning of the Trimethylaluminum (TMAl)/Triethylgallium (TEGa) molar flow rate ratio and growth temperature. High crystalline quality with pure β-phase $(Al_xGa_{1-x})_2O_3$ was achieved for films with Al composition x< 27%, while higher Al composition induced phase segregation which was observed via X-ray diffraction spectra. Al incorporation was highly dependent on the growth temperature, chamber pressure, oxygen partial pressure and TMAl molar flow rate. Atomic resolution scanning transmission electron microscopy (STEM) imaging demonstrated a high crystalline quality β-$(Al_{0.15}Ga_{0.85})_2O_3$ film with epitaxial interface. High resolution STEM (HRSTEM) imaging of $(Al_xGa_{1-x})_2O_3/Ga_2O_3$ superlattice (SL) structures revealed superior crystalline quality for 23% Al composition. When Al composition reaches 40%, the SL structure maintained β-phase but the interfaces became rough with inhomogeneous Al distribution. N-type doping using Si in β-$(Al_xGa_{1-x})_2O_3$ films with Al composition up to 33.4% was demonstrated.

Keywords: Ultra-wide bandgap, β-$(Al_xGa_{1-x})_2O_3$ thin films, metalorganic chemical vapor deposition, AlGaO/GaO superlattice

Having a large energy bandgap (4.5-4.9 eV) [1, 2], predicted high breakdown field strength (6-8 MV/cm) [1], and capability for n-type doping, β-Ga_2O_3 is considered a promising semiconductor candidate for advancing power electronics and short wavelength optoelectronics. The availability of Ga_2O_3 native substrates via melt growth methods [3-5] enables high quality epitaxy of thin films [6-9] and structures for high performance device applications, including lateral field-effect transistors [10,11], high-breakdown Schottky barrier diodes [12.13] and vertical transistors [14,15].

Band gap engineering by alloying Ga_2O_3 with Al_2O_3 can ideally expand the accessible energy band gap of $(Al_xGa_{1-x})_2O_3$ from 4.5-4.9 eV (x=0) to 8.8 eV (x=1) [16]. Hill et al. predicted the solubility limit of Al_2O_3 in β-Ga_2O_3 to be 67% at ~1625°C based on the equilibrium phase diagram of Ga_2O_3-Al_2O_3 alloy [17]. However, experimental demonstration is still lacking. Lateral field effect transistors using AlGaO/GaO heterostructures grown by molecular beam epitaxy (MBE) have been demonstrated with a maximum Al composition of 16% [18]. Modulation doped field effect transistor (MODFET) with 2D electron gas (2DEG) sheet charge density of 2 x 10^{12} cm^{-2}, room temperature mobility of 180 $cm^2/V{\cdot}s$ and low temperature peak mobility of 2790 $cm^2/V{\cdot}s$ was demonstrated by the formation of AlGaO/GaO 2DEG channel with 18% Al content [19]. In order to achieve 2DEG with higher sheet charge density, a larger band offset at AlGaO/GaO interface for better carrier confinement is required. Therefore, it is in great need to develop high quality epitaxy of AlGaO with higher Al composition. In addition, n-type doping and transport properties in AlGaO have not been reported previously.

Previous efforts on the growth of AlGaO alloys include MBE [19-23], mist chemical vapor deposition (CVD) [24–26], pulsed laser deposition (PLD) [27-30], and metalorganic chemical vapor deposition (MOCVD) [31]. However, studies on the growth of single crystalline β-$(Al_xGa_{1-}$

$_x)_2O_3$ thin films are still limited. The most recent studies from MBE growth indicated that the phase stability of Al_2O_3 in β-Ga_2O_3 was limited to ~18% due to the formation of $AlGaO_3$ intermediate compound at temperature ranging between 600-800°C [21]. A recent report on the MOCVD growth of AlGaO showed Al incorporation up to 43% based on optical transmission spectra measurements [31]. The demonstration of high crystalline quality β-AlGaO with high Al composition and comprehensive characterization especially at atomic scale are still lacking.

In this study, we investigated the MOCVD growth of (010) β-$(Al_xGa_{1-x})_2O_3$ thin films on Fe doped semi-insulating (010) β-Ga_2O_3 substrates (from Novel Crystal Technology, Inc.). N-type doping of β-$(Al_xGa_{1-x})_2O_3$ thin films were demonstrated. Triethylgallium (TEGa) and Trimethylaluminum (TMAl) were used as the metalorganic precursors for Ga and Al, respectively, and pure O_2 was used as the O precursor. Diluted silane was used as the n-type dopant source. A typical substrate temperature ranged between 825°C and 920°C, and growth chamber pressure was tuned between 20 to 80 Torr. The group VI/III ratio was varied from 880 to 1760.

The crystalline quality and surface morphology of β-$(Al_xGa_{1-x})_2O_3$ films were characterized by high-resolution X-ray diffraction (HRXRD, Bruker D8 Discover), scanning electron microscopy (SEM, FEI Helios 600) and atomic force microscopy (AFM, Bruker AXS Dimension Icon). The room temperature electron mobility and carrier concentrations of Si doped β-AlGaO films with different Al compositions were measured by Ecopia HMS 3000 Hall measurement system. Ti/Au with thickness of 30/200 nm were deposited on the four corners of the samples for van der Pauw Hall measurement. High-angle annular dark-field scanning transmission electron microscopy (HAADF-STEM, Thermofisher probe-corrected Titan STEM, 300 kV) with atomic

resolution was used to characterize the β-AlGaO films, the AlGaO/GaO interfaces and AlGaO/GaO superlattice (SL) structures.

(010) β-$(Al_xGa_{1-x})_2O_3$ thin films with different Al compositions were grown by tuning the TEGa/TMAl molar ratio at 880 °C. Increasing the TMAl molar flow rate effectively increased the Al compositions in β-$(Al_xGa_{1-x})_2O_3$ films from 10% to 40%. Figure 1 shows the XRD ω-2θ scan spectra for (010) β-$(Al_xGa_{1-x})_2O_3$ thin films with thickness of ~ 800 nm. The (020) β-Ga_2O_3 peak corresponded to the signal from the Ga_2O_3 substrates. As the Al composition x increased, the separation between the peaks corresponding to the (020) β-$(Al_xGa_{1-x})_2O_3$ epilayer and the (020) β-Ga_2O_3 substrate increased which is due to the reduction of the spacing between the (020) planes as the atomic radius of Al is smaller than that of the Ga [20]. As the Al composition x increased, the reduction of XRD peak intensity and increase of the linewidth indicated the degradation of the crystalline quality of the β-$(Al_xGa_{1-x})_2O_3$ epilayer. However, the reduction of the peak intensity can also be partially contributed by the lower X-ray scattering factor for Al than Ga, resulting in weaker x-ray diffractions for β-$(Al_xGa_{1-x})_2O_3$ films with higher Al contents [25]. In addition to the (020) β-$(Al_xGa_{1-x})_2O_3$ peak, another peak appeared at $2\theta = \sim 65°$ when the Al composition x> 27%. This peak was believed to be related to phase segregation, which was also observed in MBE grown β-$(Al_xGa_{1-x})_2O_3$ films [21], and the physical origin of this peak still requires further investigation.

The surface morphologies of the (010) β-$(Al_xGa_{1-x})_2O_3$ films were characterized by FESEM and AFM images. Figures 2(a)-(c) represent the FESEM images of the (010) β-$(Al_xGa_{1-x})_2O_3$ films with different Al composition at x = 10%, 27%, and 40%, respectively. All films show uniform morphologies across the entire surfaces of the samples. The characterized $(Al_xGa_{1-x})_2O_3$ films have a similar thickness of ~800 nm. Figure 2(a) exhibits a smooth and featureless surface of the film with an Al composition of 10%. When the Al composition increased to 27%, as shown in Fig. 2(b),

the surface roughness increases and a similar surface morphology was observed for the film with Al composition of 40% as shown in Fig. 2(c). To better characterize the surface feature and roughness, AFM was carried out for the same films with a scanning area of 5 μm x 5 μm as shown in Fig. 2(d)-(f). For the β-$(Al_{0.1}Ga_{0.9})_2O_3$ film, the RMS roughness was low at 0.51 nm (Fig. 2(d)). For the β-$(Al_{0.27}Ga_{0.73})_2O_3$ film, the RMS roughness increased to 22.8 nm with visible grains (Fig. 2(e)). When the Al composition increased to 40%, the RMS roughness was decreased to 6.6 nm, which was due to the reduced grain size as shown in Fig. 2(f). The trend of the surface roughness as a function of the Al composition can be related to the observed phase segregation for the films with Al composition >27%.

To investigate the crystalline properties of the MOCVD grown (010) β-$(Al_xGa_{1-x})_2O_3$ materials at the atomic scale, β-$(Al_xGa_{1-x})_2O_3$ thin films and AlGaO/GaO superlattice (SL) structures with different Al composition were characterized using atomic resolution HAADF-STEM. Figure 3(a) shows the STEM imaging of the (010) β-$(Al_{0.15}Ga_{0.85})_2O_3$ thin film from the $[001]_m$ zone axis. The dark contrast of the 193 nm epifilm indicates the presence of Al as the intensity in the HAADF STEM image depends on the atomic number of the elements present [21]. The epifilm displays a uniform cross-section without extended defects. Atomic resolution imaging at the interface (Fig. 3(b)) and in the β-$(Al_{0.15}Ga_{0.85})_2O_3$ layer (Fig. 3(c)) confirmed the epitaxial growth of (010) β-$(Al_{0.15}Ga_{0.85})_2O_3$ on top of (010) Ga_2O_3 substrate.

Although free of extended defects, the β-$(Al_xGa_{1-x})_2O_3$ films were further probed for point defects using atomic resolution STEM imaging. Point defect complexes have recently been identified and shown to contribute to compensation in bulk β-Ga_2O_3 [32]. The same defect complexes are also observed here in the β-$(Al_xGa_{1-x})_2O_3$ films in the $[001]_m$ imaging orientation. Figure 4 shows a STEM image of β-$(Al_{0.40}Ga_{0.60})_2O_3$/β-$Ga_2O_3$ with a string of point defect

complexes in the β-$(Al_{0.40}Ga_{0.60})_2O_3$ film. These point defect complexes are comprised of two Ga vacancies and a Ga interstitial which is located directly between the vacancies [33]. In the image, the cation interstitials are clearly distinguishable, while the two adjacent Ga columns display decreased intensity from the vacancies located within the columns. These divacancy – cation interstitial defect complexes have been shown to act as deep acceptors, creating a trap state at E_C-2.0 eV [34]. Their development, recognized to be facilitated by doping through increased vacancy concentrations [32], will require further consideration as the films examined here are exclusively alloyed.

Two SL structures with calibrated Al compositions were grown. Figures 5(a) and 5(b) show STEM imaging of the β-$(Al_{0.23}Ga_{0.77})_2O_3$/β-$Ga_2O_3$ SL with 8 periods and AlGaO barrier layer and GaO well thicknesses of ~7.4 nm and 14.3 nm, respectively. A UID β-Ga_2O_3 buffer layer with thickness of 65 nm was grown prior to the growth of the SL structures. Atomic resolution imaging (Fig. 5(b)) demonstrated epitaxial growth with uniform Al distribution in the AlGaO layer. Figures 5(c) and 5(d) show the STEM imaging of the β-$(Al_{0.4}Ga_{0.6})_2O_3$/β-Ga_2O_3 SL with AlGaO barrier thickness of 11.5 nm and GaO thickness of 14.3 nm. The uniformity of the layer structures degraded and the interfaces between AlGaO/GaO became rough as the growth proceeded as shown in Fig. 5(c). From the atomic resolution image shown in Fig. 5(d), nonuniform contrast in the AlGaO layers was clearly observed depicting a nonuniform distribution of Al, although the β-phase lattice structure was maintained in the first few layers.

Figures 6(a) and 6(b) plot the XRD ω-2θ scan spectra for the two SL structures grown with Al compositions of 23% and 40%, respectively. The presence of the equally distanced satellite peak pattern confirm the periodic SL structures. As shown in Fig. 6(a), the sharp and distinguishable high order satellite peaks along with strong 0^{th} order peak indicate sharp

AlGaO/GaO interfaces and high quality uniform alloy composition in the AlGaO layers. The average Al compositions derived from 0^{th} order peak position and the SL period determined by using the angular separation between two adjacent peaks [35] for the SL structure with 23% Al content are 7.5% and 20.7 nm, respectively. These results are in a good agreement with the values estimated by using the barrier and well thicknesses from STEM images (average Al composition of 7.8% and SL period of 21.7 nm). The average Al composition of 12% and the SL period of 25.7 nm for 40% AlGaO/GaO SL structure were derived from the position of 0^{th} order and the satellite peaks as shown in Fig. 6(b). As observed from the STEM image (Fig. 5(c)), the nonuniformity of the layer thicknesses and the inhomogeneity of the alloy compositions especially in the upper layers cause the decrease of satellite peak intensity and periodicity.

N-type doping of β-$(Al_xGa_{1-x})_2O_3$ using Si as dopant was demonstrated via MOCVD. The room temperature electron mobility vs. carrier concentration for β-$(Al_xGa_{1-x})_2O_3$ with x varying between 6.3% and 33.4 % is shown in Fig. 7. Controllable n type doping concentration from low -10^{17} cm^{-3} to low-10^{18} cm^{-3} for β-$(Al_xGa_{1-x})_2O_3$ thin films was achieved by systematic tuning of the silane flow rate. The general trend indicates that Si incorporation efficiency decreases as Al composition increases. The physical mechanism requires further investigation. From Fig. 7, the room temperature mobilities decrease with increasing carrier concentration. With Al composition x = 23.3%, the room temperature mobility of 108 $cm^2/V{\cdot}s$ was achieved with a doping concentration of 1.36 x 10^{17} cm^{-3}.

In conclusion, β-$(Al_xGa_{1-x})_2O_3$ MOCVD growths on Ga_2O_3 substrates were demonstrated with Al incorporation up to 40%. High crystalline quality AlGaO/GaO SL structures were confirmed from HRSTEM imaging and XRD measurements. Al composition inhomogeneity was observed in films with relatively high Al composition. Interstitial point defects at the atomic

resolution was observed in the MOCVD grown β-$(Al_xGa_{1-x})_2O_3$ films. N-type doping of β-$(Al_xGa_{1-x})_2O_3$ using Si as dopant was demonstrated for films with Al composition up to 33.4%. Room temperature mobility of 108 $cm^2/V{\cdot}s$ was achieved for β-$(Al_{0.23}Ga_{0.77})_2O_3$ with a doping concentration of $1.36x10^{17}$ cm^{-3}. The advancement on MOCVD epitaxy of β-$(Al_xGa_{1-x})_2O_3$ thin films and demonstration of n-type doping will harness this emerging ultrawide bandgap semiconductor for power electronics.

Acknowledgements

The authors acknowledge the funding support from the Air Force Office of Scientific Research FA9550-18-1-0479 (AFOSR, Dr. Ali Sayir). Feng and Zhao also acknowledge partial support from the National Science Foundation (1810041).

References:

1. M. Higashiwaki, K. Sasaki, A. Kuramata, T. Masui, and S. Yamakoshi, Appl. Phys. Lett. 100, 013504 (2012).
2. H. Peelaers, C.G. Van de Walle, Phys. Status Solidi B 252, 828 (2015).
3. N. Ueda, H. Hosono, R. Waseda, and H. Kawazoe, Appl. Phys. Lett. 71, 933 (1997).
4. Y. Tomm, P. Reiche, D. Klimm, and T. Fukuda, J. Cryst. Growth 220, 510 (2000).
5. H. Aida, K. Nishiguchi, H. Takeda, N. Aota, K. Sunakawa, and Y. Yaguchi, Jpn. J. Appl. Phys. 47, 8506 (2008).
6. Z. Feng, A F M A. U. Bhuiyan, M. R. Karim, and H. Zhao, Appl. Phys. Lett. 114, 250601 (2019).
7. M. Baldini, M. Albrecht, A. Fiedler, K. Irmscher, R. Schewski, and G. Wagner, 304 ECS J. Solid State Sci. Technol. 6, Q3040 (2017).
8. S. Rafique, L. Han, M. J. Tadjer, J. A. Freitas Jr, N. A. Mahadik, and H. Zhao, Appl. Phys. Lett. 108, 182105 (2016).
9. H. Okumura, M. Kita, K. Sasaki, A. Kuramata, M. Higashiwaki, and J. S. Speck, Appl. Phys. Express 7, 095501 (2014).
10. M. H. Wong, K. Sasaki, A. Kuramata, S. Yamakoshi, and M. Higashiwaki, IEEE Electron Device Lett. 37, 212 (2016).
11. J. Green, K. D. Chabak, E. R. Heller, R. C. Fitch, Jr., M. Baldini, A. Fiedler, K. Irmscher, G. Wagner, Z. Galazka, S. E. Tetlak, A. Crespo, K. Leedy, and G. H. Jessen, IEEE Electron Dev. Lett. 37, 902 (2016).
12. J. Yang, F. Ren, M. Tadjer, S. J. Pearton, and A. Kuramata, ECS J. Solid State Sci. Technol. 7, Q92 (2018).
13. W. Li, Z. Hu, K. Nomoto, R. Jinno, Z. Zhang, T. Q. Tu, K. Sasaki, A. Kuramata, D. Jena, and H. G. Xing, 2018 IEEE International Electron Devices Meeting (IEDM) pp. 8.5.1 (2018).
14. M. H. Wong, K. Goto, H. Murakami, Y. Kumagai, and M. Higashiwaki, IEEE Electron Device Lett. 40, 3 (2019).
15. Z. Hu, K. Nomoto, W. Li, N. Tanen, K. Sasaki, A. Kuramata, T. Nakamura, D. Jena and H. G. Xing; IEEE Electr. Device L. 39, 869 (2018).
16. H. Peelaers, J. B. Varley, J. S. Speck, and C. G. Van de Walle, Appl. Phys. Lett. 112, 242101 (2018).
17. V.G. Hill, R. Roy, and E.F. Osborn, J. Am. Ceram. Soc. 35, 135 (1952).
18. H. Okumura, Y. Kato, T. Oshima and T. Palacios, Jpn. J. Appl. Phys. 58, SBBD12 (2019).
19. Y. Zhang, A. Neal, Z. Xia, C. Joishi, J. M. Johnson, Y. Zheng, S. Bajaj, M. Brenner, D. Dorsey, K. Chabak, G. Jessen, J. Hwang, S. Mou, J. P. Heremans, and S. Rajan, Appl. Phys. Letts. 112, 173502 (2018).
20. T. Oshima, T. Okuno, N. Arai, Y. Kobayashi, and S. Fujita, Jpn. J. Appl. Phys. 48, 070202 (2009).
21. S. W. Kaun, F. Wu, J. S. Speck, J. Vac. Sci. Technol. A, 33, 041508 (2015).

22. T. Oshima, Y. Kato, N. Kawano, A. Kuramata, S. Yamakoshi, S. Fujita, T. Oishi, and M. Kasu, Appl. Phys. Express 10, 035701 (2017).
23. E. Ahmadi, Y. Oshima, F. Wu and J. S. Speck, Appl. Phys. Express 10, 071101 (2017).
24. H. Ito, K. Kaneko and S. Fujita, Jpn. J. Appl. Phys. 51, 100207 (2012).
25. K. Kaneko, K. Suzuki, Y. Ito, and S. Fujita, J. Cryst. Growth 436, 150 (2016).
26. S.-D. Lee, Y. Ito, K. Kaneko, and S. Fujita, Jpn. J. Appl. Phys. 54, 030301 (2015).
27. X. Wang, Z. Chen, F. Zhang, K. Saito, T. Tanaka, M. Nishio, and Q. Guoa., AIP Adv. 6, 015111 (2016).
28. C. Kranert, M. Jenderka, J. Lenzner, M. Lorenz, H. von Wenckstern, R. Schmidt-Grund, and M. Grundmann, Appl. Phys. 117, 125703 (2015).
29. R. Schmidt-Grund, C. Kranert, H. von Wenckstern, V. Zviagin, M. Lorenz, and M. Grundmann, J. Appl. Phys. 117, 165307 (2015).
30. R. Wakabayashi, M. Hattori, K. Yoshimatsu, K. Horiba, H. Kumigashira, and A. Ohtomo, Appl. Phys. Lett. 112, 232103 (2018).
31. R. Miller, F. Alema, and A. Osinsky, IEEE Trans. Semicond. Manuf. 31(4), 467 (2018).
32. J. M. Johnson, Z. Chen, J. B. Varley, C. M. Jackson, E. Farzana, Z. Zhang, A. R. Arehart, H.-L. Huang, A. Genc, S. A. Ringel, C. G. Van de Walle, D. Muller, J. Hwang, Unusual Formation of Point Defect Complexes in the Ultra-wide Bang Gap Semiconductor beta-Ga2O3, PRX 2019. arXiv:1907.00563 [cond-mat.mtrl-sci]
33. J. B. Varley, H. Peelaers, A. Janotti and C. G. Van de Walle, J. Phys. Condens. Matter 23, 334212 (2011).
34. E. Farzana, M. F. Chaiken, T. E. Blue, A. R. Arehart and S. A. Ringel, APL Mater. 7, 022502 (2019).
35. T.-C.Wen and W.-I. Lee, Jpn. J. Appl. Phys. 40, 5302 (2001).

Figure Caption

Figure 1 XRD ω-2θ scan profiles for (010) β-$(Al_xGa_{1-x})_2O_3$ films grown on (010) β-Ga_2O_3 substrates with various Al compositions. XRD peaks corresponding to 10%, 15%, 18%, 27% and 40% of Al compositions were identified.

Figure 2 Surface view FESEM images of β-$(Al_xGa_{1-x})_2O_3$ films (~800 nm) with (a) x = 10%, (b) x = 27% and (c) x = 40%. The corresponding AFM images (5 μm x 5 μm) of β-$(Al_xGa_{1-x})_2O_3$ films with (a) x = 10%, (b) x = 27% and (c) x = 40%.

Figure 3 High resolution HAADF-STEM images taken from the $[001]_m$ zone axis projection of the β-$(Al_{0.15}Ga_{0.85})_2O_3$ film (~193 nm) grown on (010) β-Ga_2O_3 substrate at (a) 50 nm, (b) 5 nm, and (c) 2 nm scale. Subscript 'm' represents the 'monoclinic' structure.

Figure 4 Crystal structure for $[001]_m$ β-Ga_2O_3 and atomic resolution STEM image of β-$(Al_{0.4}Ga_{0.6})_2O_3$/β-Ga_2O_3 showing divacancy – cation interstitial defect complexes. The red x in the model indicates the position of the cation interstitials. Three point defect complexes are marked in the image with the red arrows pointing to the cation interstitials and the green arrows pointing to the vacancy containing Ga columns.

Figure 5 High resolution HAADF-STEM images of the 8-period β-$(Al_xGa_{1-x})_2O_3$/β-Ga_2O_3 SLs cross-section grown on (010) β-Ga_2O_3 substrate with Al composition of (a, b) 23% and (c, d) 40% at (a, c) 50 nm and (b, d) 2 nm scale.

Figure 6 XRD ω-2θ scan profiles for β-$(Al_xGa_{1-x})_2O_3$/β-Ga_2O_3 SLs grown on (010) β-Ga_2O_3 substrates with Al composition of (a) 23% and (b) 40%.

Figure 7 Room temperature Hall mobility vs. carrier concentration for (010) β-$(Al_xGa_{1-x})_2O_3$ films grown on β-Ga_2O_3 (010) substrates with various Al compositions.

Figure 1

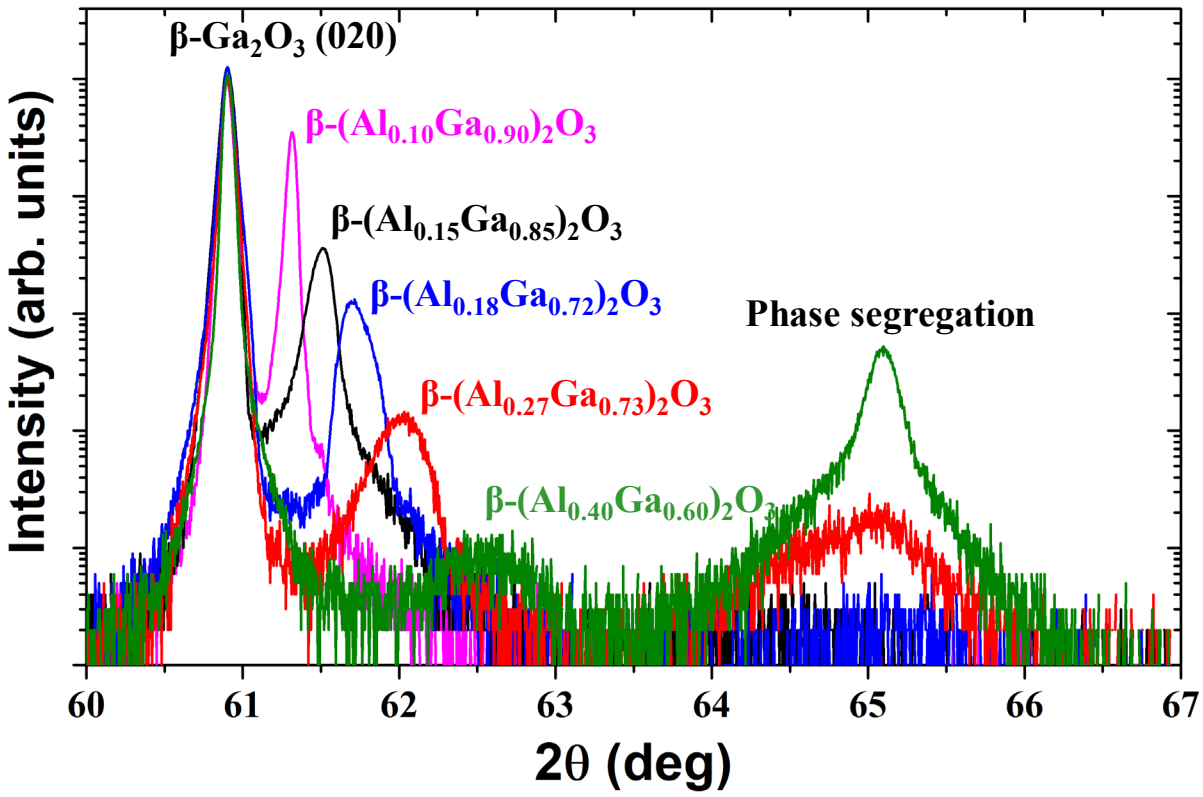
β-Ga2O3 (020)
β-(Al0.10Ga0.90)2O3
β-(Al0.15Ga0.85)2O3
β-(Al0.18Ga0.72)2O3
β-(Al0.27Ga0.73)2O3
β-(Al0.40Ga0.60)2O3
Phase segregation
Intensity (arb. units)
60
61
62
63
64
65
66
67
2θ (deg)

Figure 2

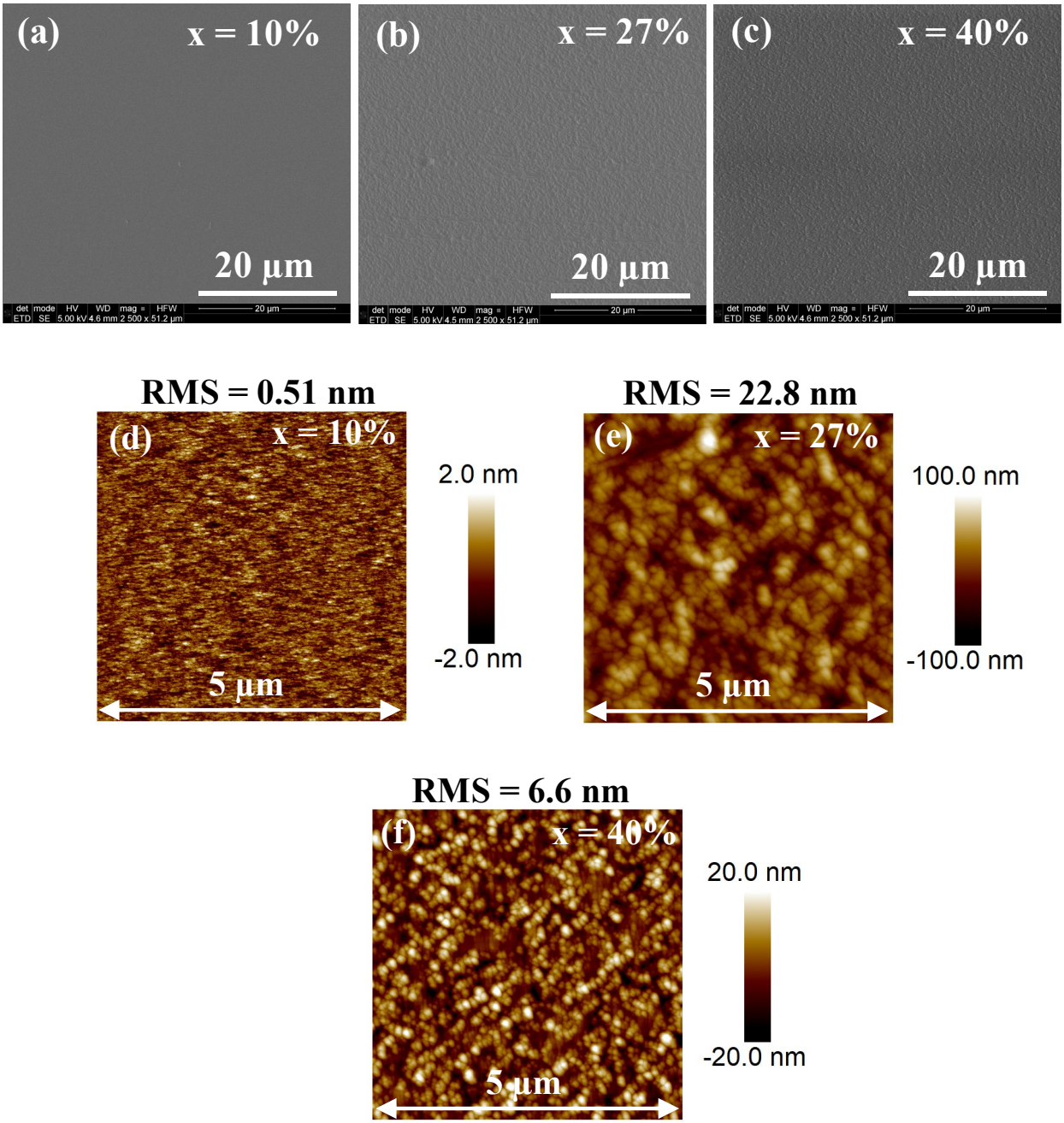
(a)
x = 10%
20 µm
(b)
x = 27%
20 µm
(c)
x = 40%
20 µm
RMS = 0.51 nm
(d)
x = 10%
5 µm
2.0 nm
-2.0 nm
RMS = 22.8 nm
(e)
x = 27%
5 µm
100.0 nm
-100.0 nm
RMS = 6.6 nm
(f)
x = 40%
5 µm
20.0 nm
-20.0 nm

Figure 3

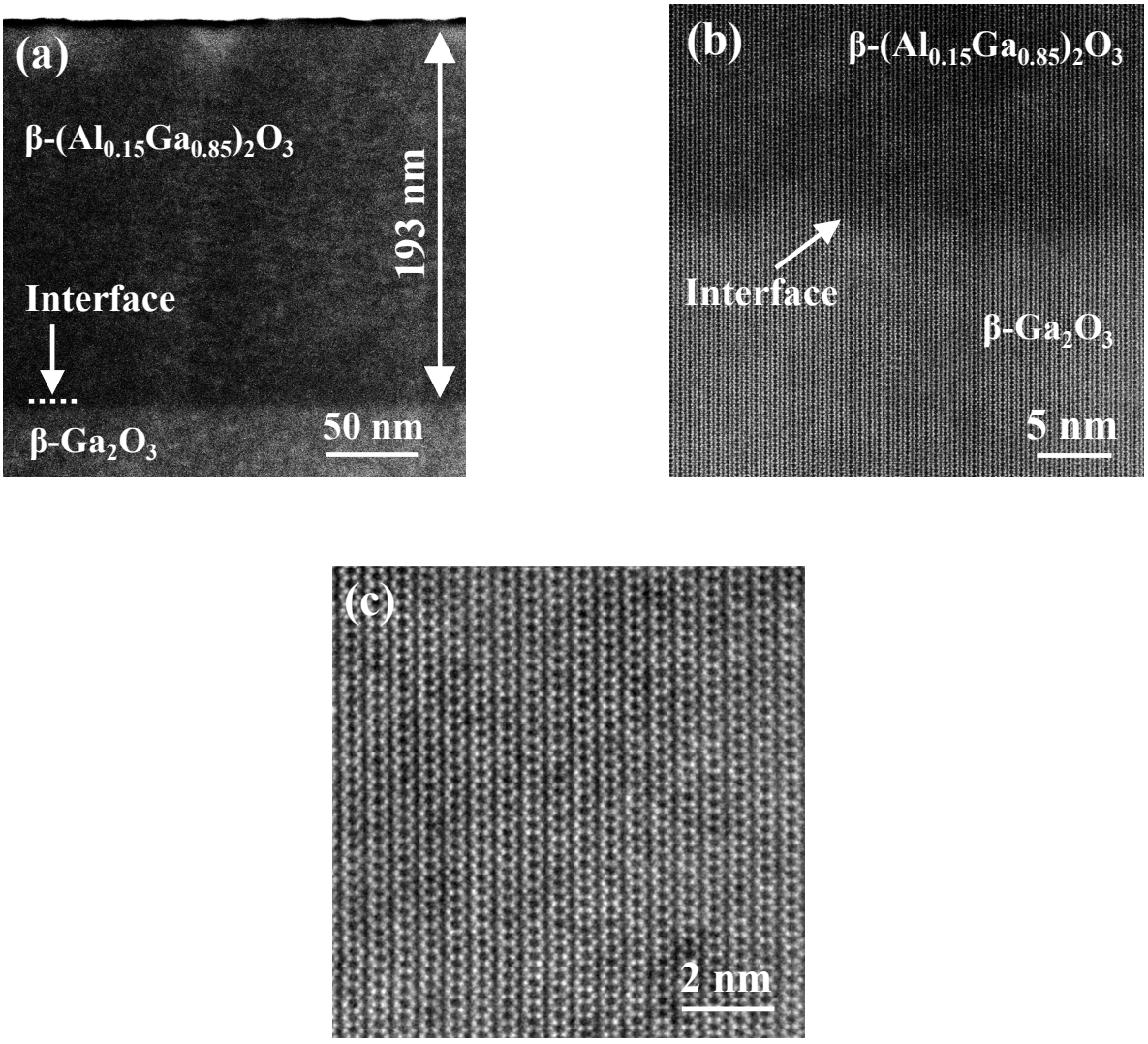
(a)
β-(Al0.15Ga0.85)2O3
193 nm
Interface
β-Ga2O3
50 nm
(b)
β-(Al0.15Ga0.85)2O3
Interface
β-Ga2O3
5 nm
(c)
2 nm

Figure 4

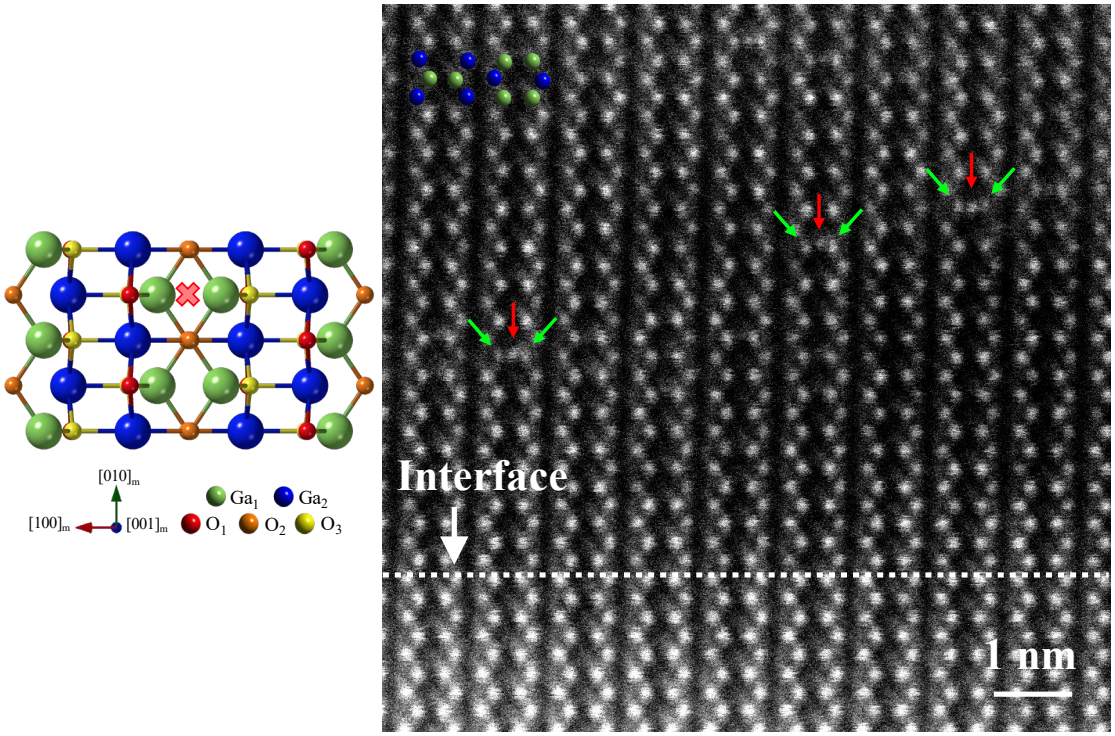

Figure 5

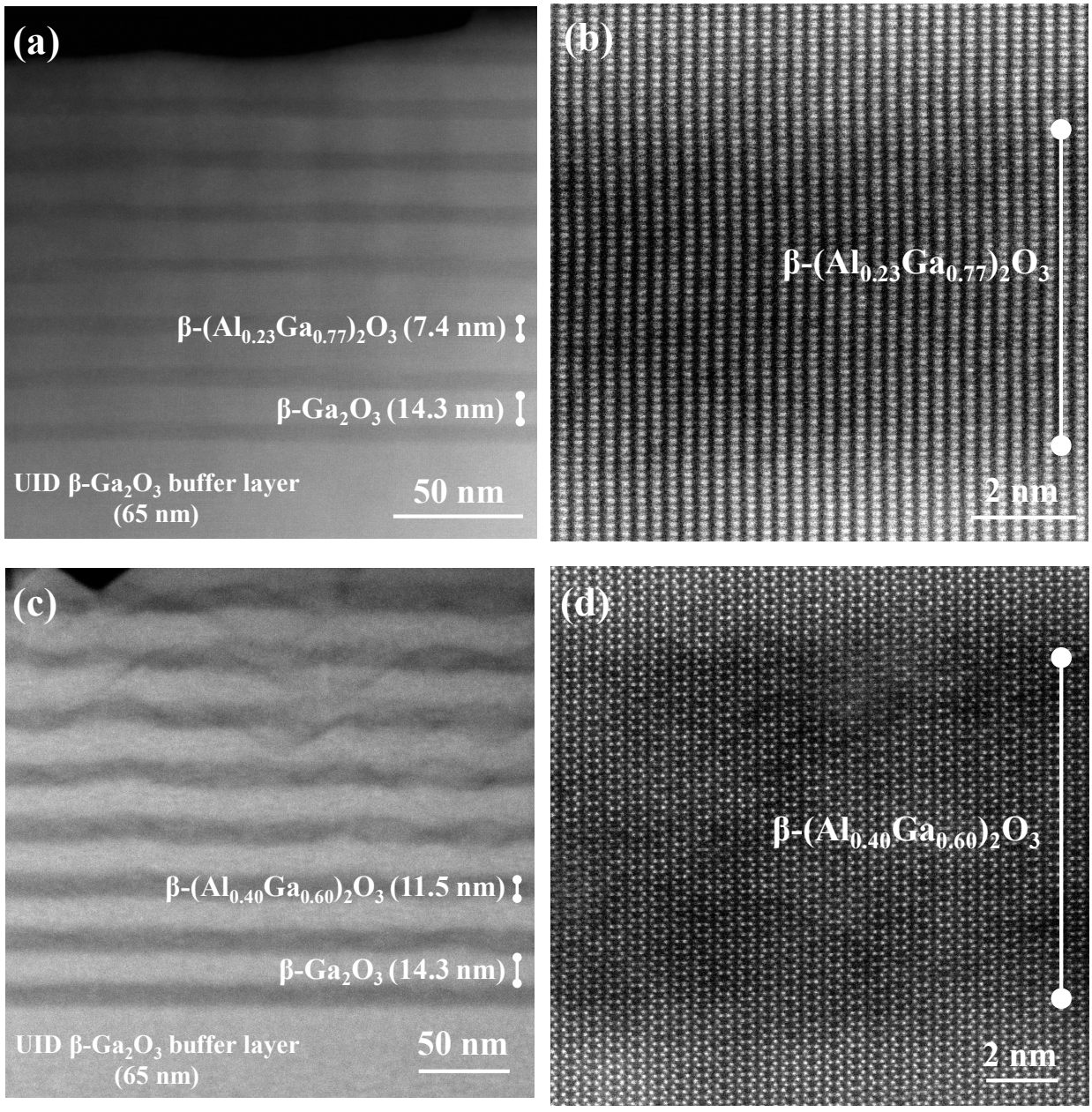
(a)
β-(Al0.23Ga0.77)2O3 (7.4 nm)
β-Ga2O3 (14.3 nm)
UID β-Ga2O3 buffer layer (65 nm)
50 nm
(b)
β-(Al0.23Ga0.77)2O3
2 nm
(c)
β-(Al0.40Ga0.60)2O3 (11.5 nm)
β-Ga2O3 (14.3 nm)
UID β-Ga2O3 buffer layer (65 nm)
50 nm
(d)
β-(Al0.40Ga0.60)2O3
2 nm

Figure 6

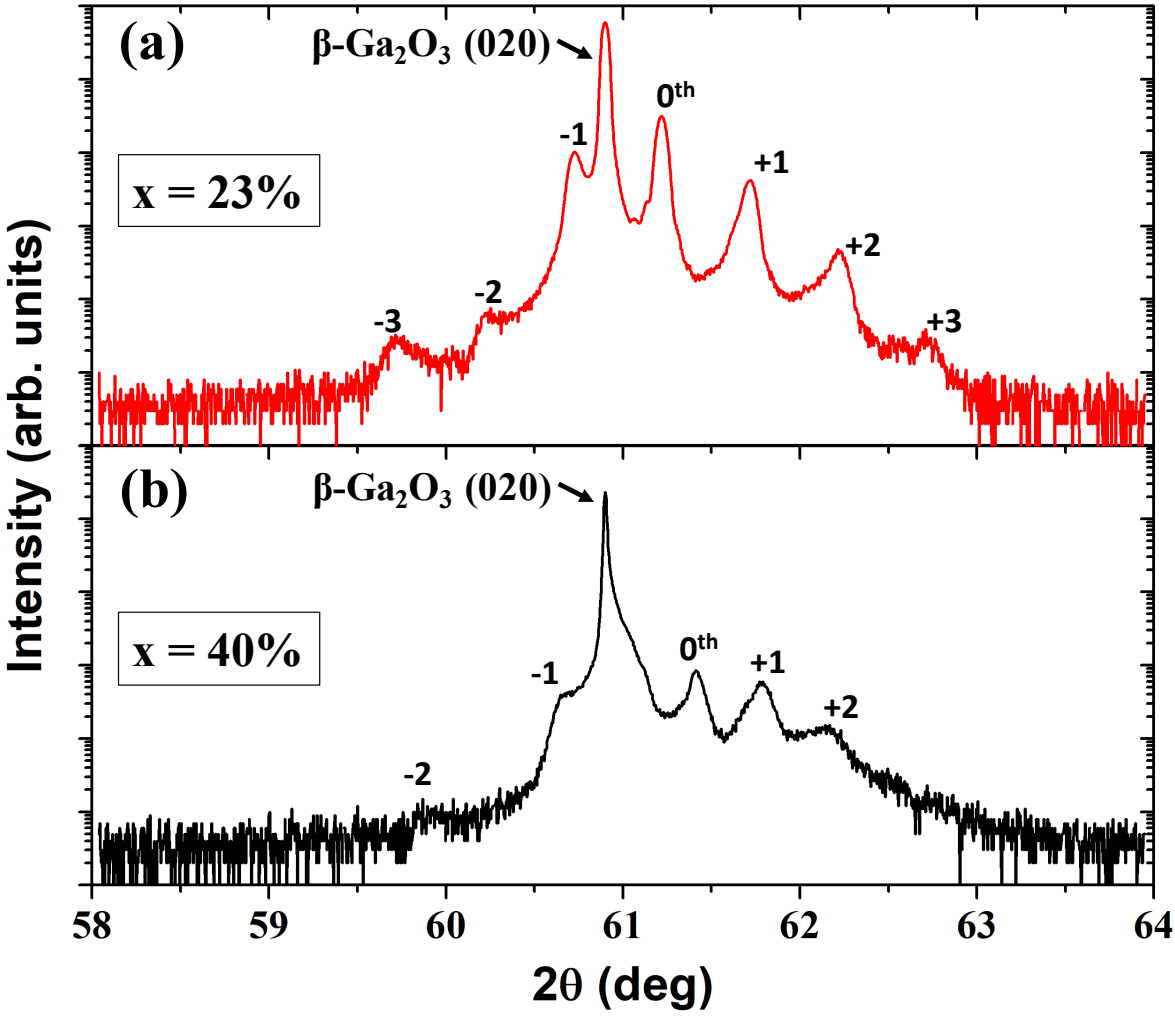
(a)
β-Ga2O3 (020)
x = 23%
-3
-2
-1
0th
+1
+2
+3
(b)
β-Ga2O3 (020)
x = 40%
-2
-1
0th
+1
+2
Intensity (arb. units)
58
59
60
61
62
63
64
2θ (deg)

Figure 7

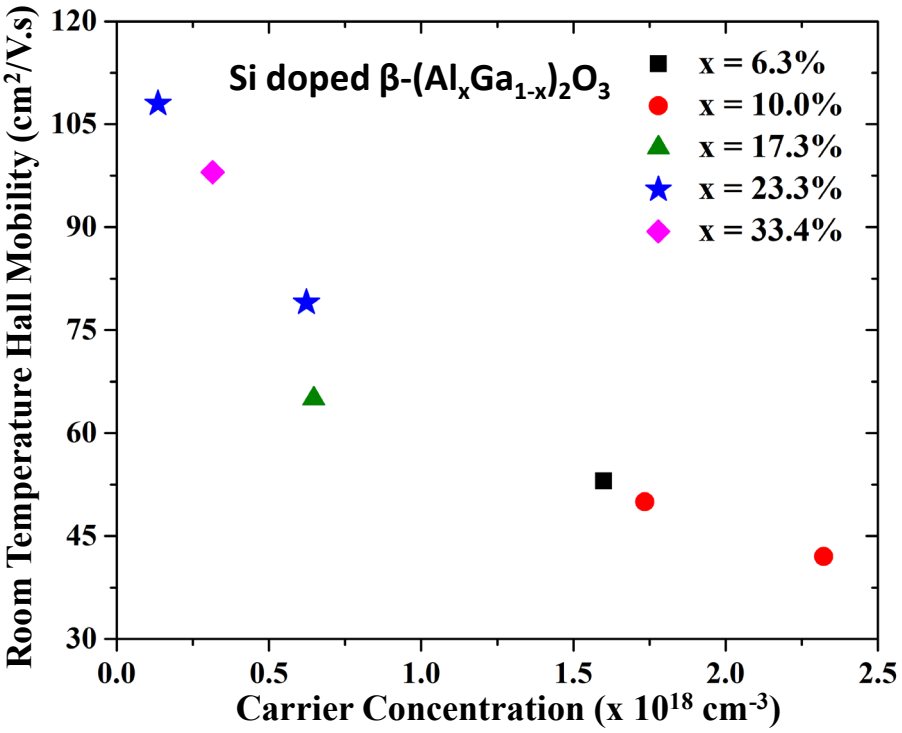
Si doped β-(Al$_x$Ga$_{1-x}$)$_2$O$_3$
x = 6.3%
x = 10.0%
x = 17.3%
x = 23.3%
x = 33.4%
Room Temperature Hall Mobility (cm^2/V.s)
Carrier Concentration (x 10^{18} cm^{-3})
120
105
90
75
60
45
30
0.0
0.5
1.0
1.5
2.0
2.5